Research Paper

In vivo tracking and quantification of inhaled aerosol using magnetic particle imaging towards inhaled therapeutic monitoring

Zhi Wei Tay[1✉], Prashant Chandrasekharan[1], Xinyi Yedda Zhou[1], Elaine Yu[2], Bo Zheng[1], Steven Conolly[1,3]

1. Department of Bioengineering, University of California, Berkeley, CA 94720, United States
2. Magnetic Insight, Inc., Alameda, CA 94501, United States
3. Department of Electrical Engineering and Computer Sciences, University of California, Berkeley, CA 94720, United States

✉ Corresponding author: Email: zwtay@berkeley.edu

Abstract

Pulmonary delivery of therapeutics is attractive due to rapid absorption and non-invasiveness but it is challenging to monitor and quantify the delivered aerosol or powder. Currently, single-photon emission computed tomography (SPECT) is used but requires inhalation of radioactive labels that typically have to be synthesized and attached by hot chemistry techniques just prior to every scan.

Methods: In this work, we demonstrate that superparamagnetic iron oxide nanoparticles (SPIONs) can be used to label and track aerosols *in vivo* with high sensitivity using an emerging medical imaging technique known as magnetic particle imaging (MPI). We perform proof-of-concept experiments with SPIONs for various lung applications such as evaluation of efficiency and uniformity of aerosol delivery, tracking of the initial aerosolized therapeutic deposition *in vivo*, and finally, sensitive visualization of the entire mucociliary clearance pathway from the lung up to the epiglottis and down the gastrointestinal tract to be excreted.

Results: Imaging of SPIONs in the lung has previously been limited by difficulty of lung imaging with magnetic resonance imaging (MRI). In our results, MPI enabled SPION lung imaging with high sensitivity, and a key implication is the potential combination with magnetic actuation or hyperthermia for MPI-guided therapy in the lung with SPIONs.

Conclusion: This work shows how magnetic particle imaging can be enabling for new imaging and therapeutic applications of SPIONs in the lung.

Key words: magnetic particle imaging, magnetic nanoparticles, lung imaging, pulmonary administration, drug delivery

Introduction

Pulmonary delivery of drugs is attractive due to benefits such as rapid absorption by the massive surface area of the alveolar region, the abundant vasculature, thin air-blood barrier, and the avoidance of first pass metabolism [1]. Monitoring the pulmonary delivery is important for evaluation of new delivery methods into the lung, new therapeutic aerosol or powder formulations and for patients with impaired, atypical lung function that may require imaging to confirm delivery. Another key application is the monitoring of slow-release formulations that need to remain long enough in the lung and resist mucociliary clearance to deliver sufficient net dosage over time.

Existing imaging techniques such as X-ray computed tomography (CT) that image the human anatomy rely on contrast agents to highlight the aerosol in the lung. While recent work on developing CT contrast agents have been promising [2,3], one key challenge is the high tissue background signal in the

body. In contrast to *in vitro* studies, *in vivo* studies require a high concentration of contrast agent to achieve a detectable change. This is difficult when imaging small amounts of aerosol spread over the lung. Conventional CT contrast agents have a sensitivity of around 1 mM [4]. However, recent work on gold nanoparticles report a CT cell tracking detection limit of 20,000 cells per μL at ~600 pg AuNP per cell [4]. Other anatomical imaging techniques such as magnetic resonance imaging (MRI) and ultrasound (US) also use contrast agents and have sensitive detection of these agents. MRI has a reported sensitivity between 0.01–1 mM and US has ~1 pM sensitivity when microbubbles are used [5]. However, both of these modalities have difficulty imaging structures containing air, such as the lung, due to air-tissue interface susceptibility changes and poor transmission of ultrasound through air, respectively.

As a result, tracer imaging modalities such as gamma scintigraphy have been the method-of-choice for imaging aerosols in the lung [6]. A tracer modality does not receive any signal from the anatomy and thus only images the tracer agent [7,8]. This enables higher sensitivity and excellent contrast. Currently, nuclear medicine imaging techniques such as positron emission tomography (PET) and gamma scintigraphy are the gold standard for *in vivo* aerosol imaging [6,9] and have reported sensitivities in the picomolar region [5]. Nuclear medicine techniques to image inhaled aerosol have been used for a multitude of clinical applications. One such clinical test is known as pulmonary radioaerosol mucociliary clearance (PRMC) test. Here, radioaerosol (nebulized 99m-technetium-albumin colloid) is inhaled and the time for the lung mucociliary clearance of this aerosol measured. This PRMC metric has been found to have high sensitivity and specificity for the disease primary ciliary dyskinesia [10,11]. Gamma scintigraphy has also been used for comparative evaluation of different aerosol formulations of asthma medication [9] as well as to evaluate the lung deposition and mucociliary clearance of inhaled therapeutic nanocarriers [12]. PET radioaerosol has been used to evaluate lung inflammation in diseases such as sarcoidosis, cystic fibrosis [13], and chronic obstructive pulmonary disease (COPD) [9].

However, there are a few limitations to nuclear medicine imaging of aerosols. One, these techniques inherently depend on the patient inhaling a radioactive tracer that poses an ionizing radiation risk, especially to the lungs, which is one of the most radiosensitive organs in the body [14, 15]. In addition, the intrinsic nuclear degradation of the radioactive tracer limits the length of mucociliary clearance

studies. The bulk of nuclear medicine studies conducted use 18F-fludeoxyglucose (FDG) with a 2 h half-life or 99m-technetium (99mTc) with a 6 h half-life [16]. While longer half-life tracers such as indium-111 (2.8 day half-life) are available [16], this incurs a larger net radiation dose to the patient or weaker SNR. Moreover, the preparation of radiopharmaceuticals is time-consuming, expensive and usually requires in-house hot chemistry facilities.
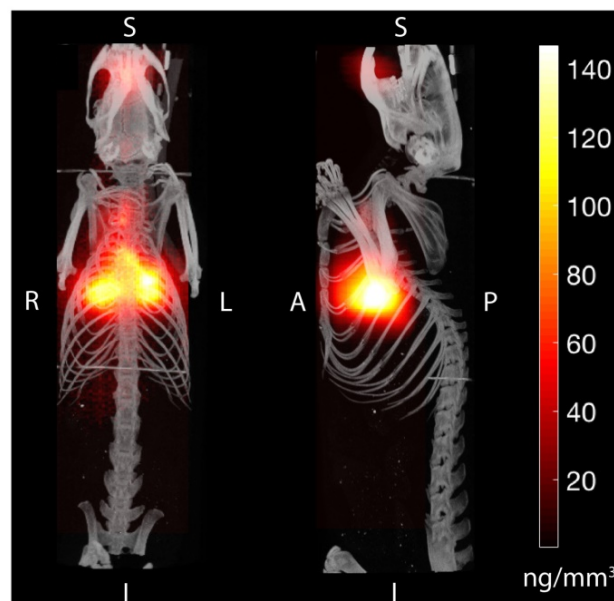
Figure 1. Magnetic particle imaging (MPI) applied to in vivo tracking of inhaled aerosol. MPI / CT imaging visualizes the in vivo distribution of the inhaled aerosol in the lung airspace (maximum intensity projection) with high contrast and sensitivity. MPI's high contrast, high sensitivity and quantitative nature enables it as a radiation-free complement to radioaerosol scintigraphy and PET for in vivo quantification of therapeutic aerosol dose and visualization of biodistribution.

To address these challenges, we propose to use magnetic particle imaging (MPI) that was invented in 2005 by Gleich and Weizenecker [17]. It produces a sensitive tracer image with zero ionizing radiation, robust imaging in the lung [8,18–20], and uses relatively safe SPIONs [21]. Because there is no signal from tissue, MPI images have very high contrast as shown in **Figure 1**. MPI images the electronic magnetization of superparamagnetic iron oxide nanoparticles (SPIONs), which is 22 million times stronger than the nuclear magnetization imaged in MRI [22]. MPI uses strong gradient magnetic fields to generate a sensitive field-free-point (or line geometry) and this is rastered over a 3D volume to form an image [22–25]. One raster trajectory is shown in **Figure 2**, but others such as the Lissajous trajectory may be used [26,27]. Image reconstruction [23,28,29] and hardware details are described in prior work [27,30,31].
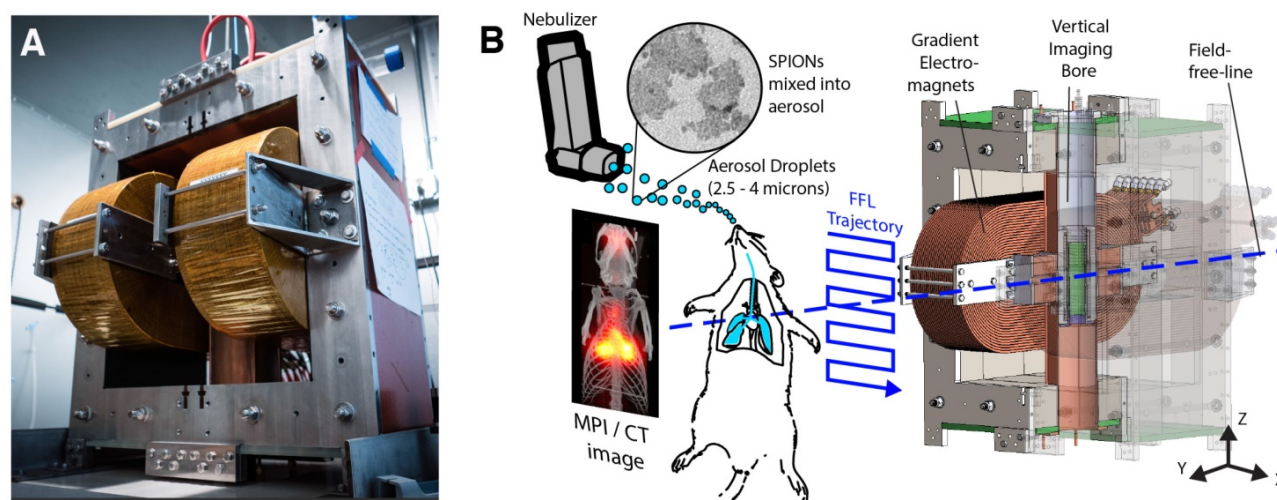
Figure 2. Hardware setup used in magnetic particle imaging (MPI) scans. (A) Photograph of the Berkeley field-free-line MPI preclinical scanner with 6.3 T/m gradient strength. **(B)** The MPI scanner uses electromagnets to generate a field-free-line (FFL) magnetic field gradient, where the effective magnetic field is zero at the line but high everywhere else. MPI can be understood as a sensitive point or sensitive line modality. When the field-free-line (FFL) is rastered across magnetic nanoparticles such as the SPIONs used here, the rapid change in SPION magnetization generates changing flux, which is picked up by the inductive receiver coil. SPIONs far away from the field-free-line remain magnetically saturated by the gradients and do not produce signal. To form a projection image, the FFL is rastered across the field-of-view with an effective trajectory as shown, thereby probing the in vivo distribution of SPIONs in the rat. Multiple projections can be used to reconstruct a 3D MPI image similar to CT.

Magnetic particle imaging has numerous advantages. First, MPI has high sensitivity and contrast [32,33]. Recent work has reported ~100 pg per 1 mm^3 voxel sensitivity [34] and high temporal resolutions of 46 frames-per-second [35]. Second, the SPIONs usable for MPI do not produce ionizing radiation, are safe and have been used in clinical applications [21,36–38]. Third, because the SPIONs are magnetic nanoparticles that do not radioactively degrade over time like radiotracers, this enables months-long longitudinal *in vivo* cell tracking studies [8,39]. This is valuable for long studies where the SPION does not enter the bloodstream and thus has a longer time before it is cleared, such as in the clinical pulmonary radioaerosol mucociliary clearance (PRMC) test. SPIONs are slow to degrade and there is no need for hot chemistry preparation of a fresh radiopharmaceutical for each new scan. Lastly, MPI is fully quantitative with zero depth attenuation as validated in prior work [22,30] thus is able to quantify the inhaled aerosol at any depth and with no view limitations since the low frequency magnetic excitation fields used in MPI penetrate completely through all types of tissue. Magnetic particle imaging has also been studied in many other applications (preclinical models) such as real-time MPI-guidance of catheters [40,41], stroke diagnosis [35], angiography [42], lung perfusion [19], lung ventilation [20,43], cancer imaging [44], stem cell tracking [8,18,45], brain perfusion imaging [46], magnetic hyperthermia [47–50] and gut bleed detection [51].

In this preclinical study, we demonstrate that MPI can track and quantify inhaled aerosol with high sensitivity and contrast and demonstrate its potential as a non-radioactive complement to nuclear medicine for evaluating mucociliary clearance and delivery efficiency of the inhaled aerosol towards inhaled therapeutic monitoring.

Methods

Nanoparticle characterization

SPIONs (Perimag™, micromod Partikeltechnologie GmbH, Rostock, Germany) was added to the aerosol mix in order to track the aerosol *in vivo* with magnetic particle imaging. These multi-core nanoparticles were prepared by precipitation of iron oxide in the presence of dextran, resulting in 50% (w/w) iron oxide in a matrix of dextran (40.000 Da molecular weight). The hydrodynamic diameter is ~130 nm with PDI < 0.25 (Zetasizer NanoZS90, Malvern Instruments Ltd., UK). Bright-field TEM (JOEL 1200 EX Transmission Electron Microscope, JEOL USA Inc., Massachusetts, USA) at 120 keV was performed and results shown in **Figure 3**. Individual cores within each multi-core cluster have average size ~5.5 ± 2 nm. The dynamic magnetization properties at MPI scanning parameters (20.225 kHz and 40 mTpp), which are more relevant to MPI performance than static magnetization, were measured by a custom-built magnetic particle spectrometer MPS as described previously [52,53]. The linearity of MPI signal with aerosol mass to validate MPI-based quantification of SPION-based aerosol is plotted in **Figure 3**C.

Aerosol inhalation setup

Details of the experimental groups are shown in **Figure 4** and the inhalation hardware setup was

constructed as shown in **Figure 5**. In short, the nebulizer was connected in line between the y-junction and the output of the rodent ventilator device to inject the aerosol into the ventilation airstream to be inhaled by the rodent. SPIONs were mixed into 1x phosphate buffered saline or the existing therapeutic formulation to a final concentration of 5 mg/mL (1.7 mg iron / mL). Due to the low concentration, the aerodynamic properties of the aerosol droplets should be negligibly affected by addition of SPIONs (< 0.5% weight change). Aerosol was generated by a vibrating mesh nebulizer (Aeroneb™ Lab Nebulizer Unit, Small VMD, Kent Scientific Corporation, Connecticut, USA) and the ventilator has tunable stroke volume and rate (Model 683 Small Animal Ventilator, Harvard Apparatus, Holliston, MA, USA).

In vitro therapeutic aerosol imaging with MPI and fluorescence imaging

The MPI agent (SPIONs) was mixed with the model drug, doxorubicin hydrochloride (DOX HCl), then aerosolized as described in the "Aerosol inhalation setup" subsection. The drug is not known to be adherent to the plain SPION dextran coating, but additional aldehyde functionalities can be added to make an acid labile linkage with the chemotherapy drug doxorubicin [54]. The aerosol was piped through the setup previously described and the output tube was filled with loose surgical gauze that allows airflow. The gauze is approximately 2 cm thick to enable deposition of aerosol on the gauze. The duration of aerosol production was varied and significant deposition was allowed before removing
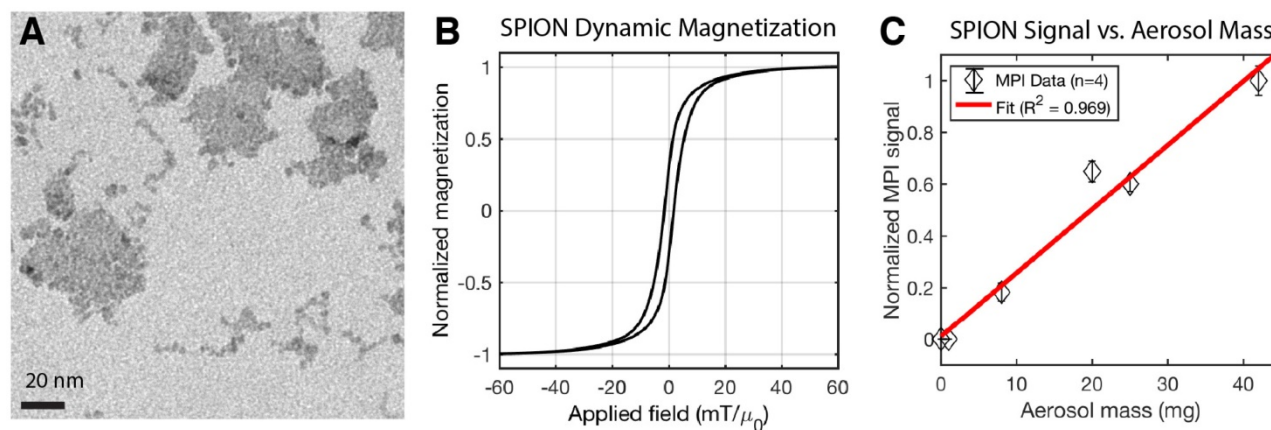
Figure 3. Characterization of the magnetic nanoparticles in magnetic particle imaging (MPI) scans. **(A)** TEM of the multi-core clustered SPIONs used. **(B)** Dynamic magnetization curves of the SPION measured at an AC excitation field of 20.225 kHz and 40 mTpp to match the MPI drive field. The saturation of the SPION magnetization at high applied field is critical for signal encoding in imaging and helps localize the received signal to the field-free-line position. **(C)** The MPI signal is well-correlated ($R^2 = 0.969$) with aerosol mass, showing that MPI is linearly quantitative for aerosol mass. MPI's quantitative nature in vivo has also been well-characterized in prior work [18,51].
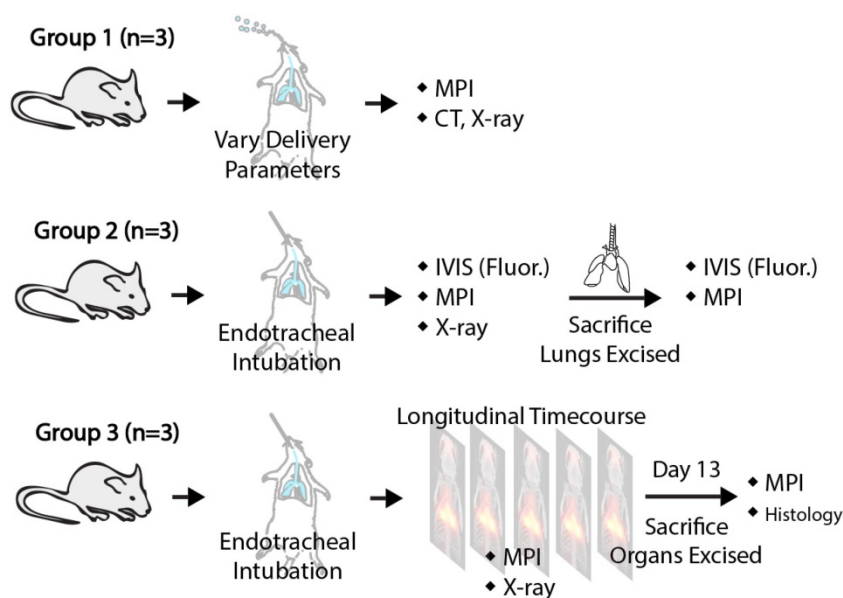
Figure 4. Illustration of the animal procedures used for the different experimental groups in this study. Group A shows how MPI can evaluate the delivery efficiency of different aerosol delivery methods. Group B verifies the correlation between MPI signal and model drug deposition to quantify drug deposition via MPI. Group C illustrates mucociliary clearance monitoring using MPI.

the gauze. The gauze was weighed with a sensitive weighing scale (Ohaus Adventurer Pro AV53) before and after the aerosol deposition to determine the weight of aerosol deposited. Subsequently, fluorescence measurements of deposited model drug (DOX HCl) was performed on the IVIS Lumina™ with Ex/Em at 525/610 nm and total exposure time was kept constant to allow quantification. Lastly, MPI was performed as described in the animal imaging section with a scan field-of-view (FOV) of 14.2 cm × 4.7 cm × 4.0 cm and scan duration of approximately 2 min. The normalized MPI signal, normalized DOX HCl fluorescence signal and aerosol mass are plotted in the correlation graphs in **Figure 3** and **Figure 5**. Because the SPIONs concentration was dilute (0.17 mg iron / mL) with respect to DOX HCl (1 mg/mL) and low concentrations were maintained while total aerosol deposited was varied, there was no observable quenching of the DOX HCl fluorescence signal by the iron oxide in the experiment.

Animal procedures

Female Fischer 344 rats (Charles River Laboratories) weighing ~200 g were used for this study. There were three experimental groups of rats as detailed in **Figure 4**. In Group A (n = 3), ~0.5 mg/kg of SPIONs was delivered by endotracheal intubation. The combination of endotracheal intubation and the small animal ventilator essentially achieves mechanical ventilation of the rat lung, enabling breathing rate and volume to be controlled by the ventilator. Variation of the aerosol droplet size and ventilator piston stroke rate was performed to affect delivery efficiency into the lung. Different aerosol droplet sizes were achieved by use of different size nebulizers. The Aeroneb™ Lab Nebulizer Unit (vibrating mesh nebulizer), Kent Scientific Corporation, Connecticut, USA comes in two sizes: a small VMD device that produces 2.5–4.0 μm aerosol droplets and a standard VMD device that produces 4.0–6.0 μm aerosol droplets. In Group B (n = 3), ~0.3 mg/kg and 0.1 mg/kg of DOX HCl from Sigma-Aldrich or indocyanine green dye (ICG) was mixed and delivered as aerosol. The rodents were imaged with MPI and fluorescence, and imaging was repeated *ex vivo* on the lungs to evaluate MPI's ability to track deposition of inhaled therapeutics in the lung. In Group C (n = 3), ~0.3 mg/kg of SPIONs were delivered into the rodents *via* aerosol inhalation and MPI scans were acquired at multiple time points up to 13 days after to evaluate clearance from the lung. For all aerosol inhalation procedures, small doses between 0.05–0.5 mg/kg were used. For comparison, up to 40 mg/kg was reported in animal studies [20] and 0.5–7.3 mg/kg in human imaging studies [55].

Aerosol was introduced either by placement of the aerosol setup output tube in the mouth cavity (with depression of the tongue), or by endotracheal intubation with controlled ventilation (stroke volume and stroke rate controlled by the small animal ventilator). These animal procedures were conducted in accordance with the National Research Council Guide for the Care and Use of Laboratory Animals and approved by the UC Berkeley Animal Care and Use Committee.

Animal imaging

For all animal imaging procedures, animals were maintained under isoflurane anesthesia (2%, 1.5 L/min) for the duration of imaging. MPI was performed with the Berkeley field-free-line (gradient of 6.3 × 6.3 T/m) MPI scanner that was validated in prior work [44] with drive (excitation) parameters of 20.225 kHz and 40 mTpp. **Figure 2B** shows the scan trajectory. Experimental group A had a field-of-view (FOV) of 3.2 cm × 4 cm × 10 cm with acquisition time of 75 s. Group B had a FOV of 3.2 cm × 4 cm × 6 cm with acquisition time of 45 s. Group C had a FOV of 3.2 cm × 4 cm × 14.1 cm with acquisition time of 115 s. X-space MPI image reconstruction [44] was used. After MPI scans were acquired, the MPI image was co-registered to anatomic reference images. Anatomic references were obtained by a projection x-ray immediately after MPI (Kubtec Xpert 40™ cabinet x-ray unit), or by a post-mortem CT scan (RS9-80 Micro CT scanner from General Electric USA at 30 min acquisition time and 93 μm isotropic resolution). To minimize position misalignment between different imaging modalities, while the animal was under isoflurane on the animal bed, the entire animal bed was transferred between the imaging modalities. MPI/CT fiducial markers that show up in both modalities were placed at corners of the animal bed to enable position alignment between the images. Fluorescence imaging was performed on the IVIS Lumina™ (Ex/Em 740/840 nm for ICG and 525/610 nm for DOX HCl).

Animal biodistribution studies

For assessment of SPION biodistribution *ex vivo*, animals from Group B and Group C were dissected post-sacrifice and the liver, spleen, heart, stomach, intestines, kidneys and lungs were harvested. The organs were imaged using MPI, with 12 cm × 4.7 cm × 4.0 cm FOV and 2 min acquisition time. For the mucociliary clearance study in Group C, the feces were also collected daily, collated and imaged with MPI using the abovementioned parameters at the stated timepoints. SPION biodistribution within each region of interest was determined in μg as mean ±

standard deviation using a calibration curve as previously described in prior MPI studies from our group [18,51].

Histology studies

For confirmation of delivery of SPION-labeled aerosol to the lung, after euthanasia and *ex vivo* imaging of the lungs, the lung was preserved in 10% formalin in preparation for histological sectioning. Hematoxylin and eosin (H&E) staining and Prussian blue staining were done to assess SPION distribution within the lung tissue.

Results

In vivo evaluation of aerosol delivery efficiency with MPI

One of the key applications of radioaerosols is the *in vivo* evaluation of aerosol delivery efficiency [9]. Here, we show that MPI is similarly able to visualize the efficiency of different delivery methods for Group A rats (**Figure 5**). It is well known from prior literature that drug-aerosol deposition depends on many factors. Inhalation flow rate, the patient's breathing pattern, particle size, and airway geometry have been shown to be most dominant [1,56]. However, particle shape, density, thermodynamic state, and surface characteristics including roughness and charge may be influential as well [57]. Here, we show that MPI can visualize the differences in efficiency resulting from two of the most dominant factors—inhalation flow rate and particle size. From prior literature, rapid inhalation increases the chance of impaction in the oropharynx and large conducting airways, while slow, steady inhalation increases the chance of penetration to the lung periphery [58]. **Figure 5B** shows that MPI can visualize this effect. With fast ventilation rate as controlled by the ventilator piston stroke rate (stroke volume and rest of ventilation

setup is kept the same), we observed a much larger fraction of aerosol deposited in the central, large conducting airways and lesser aerosol in the peripheral parts of the lung. For particle size, prior literature states the optimum is between 3 and 5 µm [59]. In **Figure 5B**, this effect is visualized with MPI. This was investigated by only changing the nebulizer mesh size (Aeroneb™ Small VMD 2.5–4.0 µm to Aeroneb™ Standard VMD 4.0–6.0 µm) while keeping the nebulizer type/brand and ventilation setup the same. The results show a large change in the deposition distribution, where there is focal deposition in the central airways and negligible aerosol reaching the outer lung. While a limited subset of all the parameters affecting drug-aerosol deposition, these examples are a proof-of-concept demonstrating the potential of MPI as a radiation-free alternative to nuclear medicine for *in vivo* evaluation of aerosol delivery efficiency.

In vivo tracking of inhaled therapeutics using MPI

Next, in order to evaluate MPI as an *in vivo* tracking agent for inhaled therapeutics, we utilized aerosols containing a mixture of both a model drug (doxorubicin hydrochloride or indocyanine green) and our SPION imaging agent. **Figure 6A** shows the experimental setup, where the mixed aerosol was tested both *in vitro* and *in vivo*. The *in vitro* results where the aerosol was produced and deposited onto surgical gauze show that the MPI signal is well-correlated with the amount of deposited DOX HCl as measured from the fluorescence signal (R^2 = 0.971). Next, we evaluated *in vivo* tracking by inhalation of this mixed aerosol in Group B rats. The MPI image clearly visualizes the *in vivo* distribution of the aerosol, while it is difficult to track the distribution with fluorescence imaging due to tissue attenuation
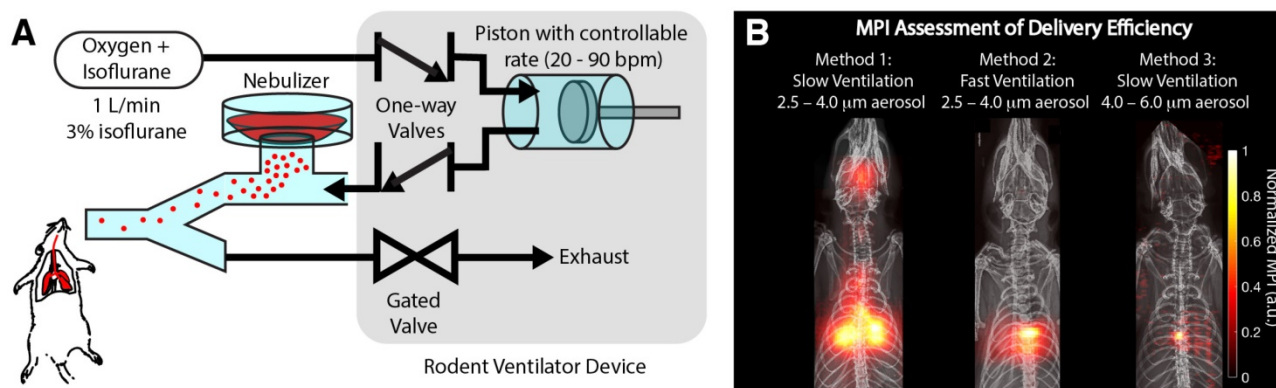
Figure 5. Magnetic particle imaging (MPI) is able to assess the delivery efficiency of different methods. (A) Experimental setup showing how the aerosol is delivered by controlled ventilation to the rodent. **(B)** MPI assessment of the delivery efficiency of three different methods. Method 1 uses a slow controlled ventilation rate. This enables the aerosol to be more evenly distributed in the lung. Method 2 uses a fast, controlled ventilation rate, resulting in more inertial impaction of the aerosol in the central conducting airways as opposed to the finer airways in the lung periphery. Method 3 increases the size of the aerosol droplets and therefore significantly increases the probability of inertial impaction in the central airways, resulting in poor delivery to lung periphery.
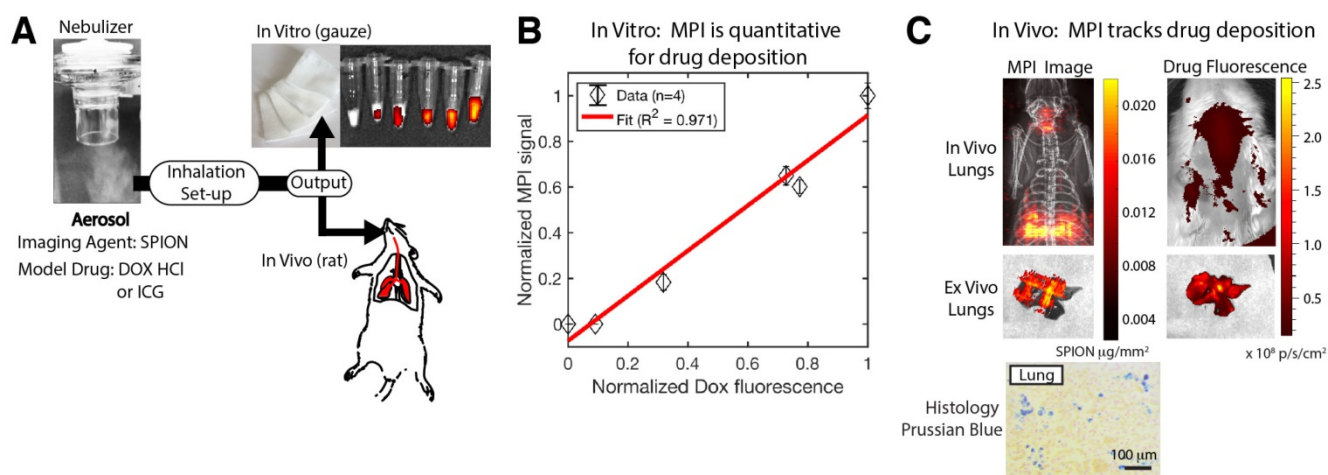
Figure 6. Magnetic particle imaging (MPI) is able to quantify the delivery of aerosolized therapeutics. (A) Experimental setup. The MPI agent (SPIONs) was mixed with the model drug, doxorubicin hydrochloride, then aerosolized. The aerosol was piped through the same inhalation setup in **Figure 5A** and the output was inhaled by the rat for the in vivo experiment or deposited on surgical gauze for the in vitro experiment. **(B)** Fluorescence measurements of deposited Dox HCl for the in vitro experiment show good correlation with the MPI signal, confirming that the MPI image can quantify drug deposition. The amount of aerosol produced and deposited on a gauze pad was varied and fluorescence and MPI of the deposited aerosol were performed as detailed in the methods section. **(C)** MPI can image at depth through tissue compared to fluorescence imaging where it is difficult to image the drug deposition at depth. Ex vivo imaging of the lungs confirms that the MPI image and the fluorescence image match, showing that MPI images the initial drug distribution in the lungs and provides clear visualization in vivo and at depth. Prussian blue staining of lung histological sections confirms presence of SPIONs in the lung.

and scatter. To address this, *ex vivo* imaging was also performed on the excised lungs. In this case, the MPI image and the fluorescence image are similar in shape and intensity, suggesting that MPI is tracking the deposition of the model drug within the lung. Slight discrepancies in position may be attributed to slight shifting of the lung lobes during transfer between the scanners. These results show the potential of MPI for quantification of therapeutic deposition in the lung towards assessment and monitoring of inhalation therapies.

### *In vivo* longitudinal MPI monitoring of mucociliary clearance of deposited aerosol

One key application of radioaerosols is the evaluation of lung mucociliary clearance. The PRMC metric obtained from 99mTc radioaerosol studies has been found to have high sensitivity and specificity for primary ciliary dyskinesia [10,11]. MPI is a good fit for imaging clearance over long periods of time because, unlike radioaerosols, the SPION imaging agent does not radioactively decay with time. This advantage has been demonstrated in prior work for the tracking of stem cells over 90 days [8]. To evaluate MPI as a tool for measuring mucociliary clearance of delivered aerosols, we allowed rats in Group C to inhale SPION aerosols and performed MPI periodically over the course of 13 days. Prior literature established that the dominant clearance of particles larger than 17 nm median diameter occurs through the mucociliary pathway up the trachea, and down the gastrointestinal tract to finally be excreted as feces from the body [20,60]. Minor clearance occurs by alveolar macrophages, but this takes a much longer time than the mucociliary pathway [61]. While it may

be possible for SPIONs to penetrate the blood-lung barrier, especially in disease states that cause higher permeability of the epithelium, the SPION coating thickness can be tailored depending on the study objective to control this possibility. The effect of particle hydrodynamic size on translocation from lung airspace into the blood has been previously studied for the size range of 2 nm to 200 nm [62], and there is negligible translocation for nanoparticle sizes 30 nm and above, which is the vast majority of hydrodynamic sizes of MPI nanoparticles. Critically, MPI performance depends on the magnetic core size, which can be kept the same to maintain performance while varying the coating thickness to control biodistribution.

The experimental results in **Figure 7** show the MPI timecourse study where the mucociliary clearance of the Perimag™ SPIONs (130 nm hydrodynamic size) from the lung into the gastrointestinal tract is clearly visualized. Due to the large hydrodynamic size, there is expected to be negligible penetration of the blood-lung barrier. At the 2 h time point, SPION boli were observed just above the lung. At the 14 h time point, SPIONs were observed in the lower gastrointestinal tract. Over the course of 13 days, the MPI signal in the lungs gradually decreased as the SPIONs were cleared from the lungs. **Figure 8A** verifies that clearance, rather than decay of the SPION signal, occurred because the loss in MPI signal from the lungs is accounted for by the presence of MPI signal in the GI tract and feces. The high contrast and sensitivity of MPI enables clear visualization of the mucociliary clearance pathway and the different organs and tissues involved.
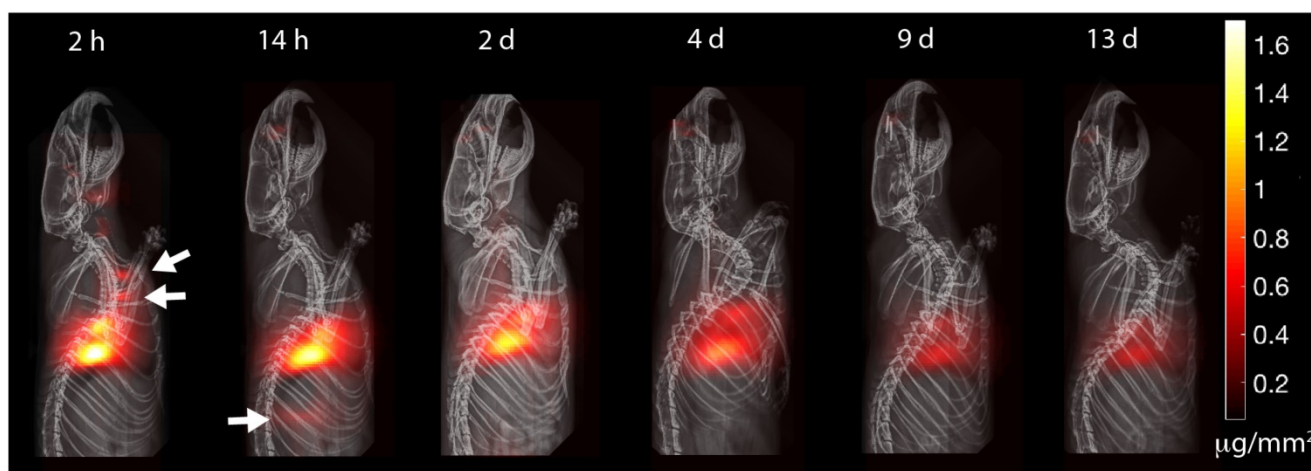
Figure 7. MPI is able to track with high contrast and sensitivity the clearance of delivered aerosol. The clearance pathway is clearly visualized by visible boli in the trachea and in the gastrointestinal tract (white arrows). Because SPIONs do not radioactively decay over time, MPI is suitable for longitudinal imaging of aerosol clearance. The visible attenuation of the signal is due to mucociliary clearance from the lung, as the lost signal is accounted for by MPI signal in excreta. MPI thus has the potential to be a radiation-free complement to current pulmonary radioaerosol mucociliary clearance clinical tests.
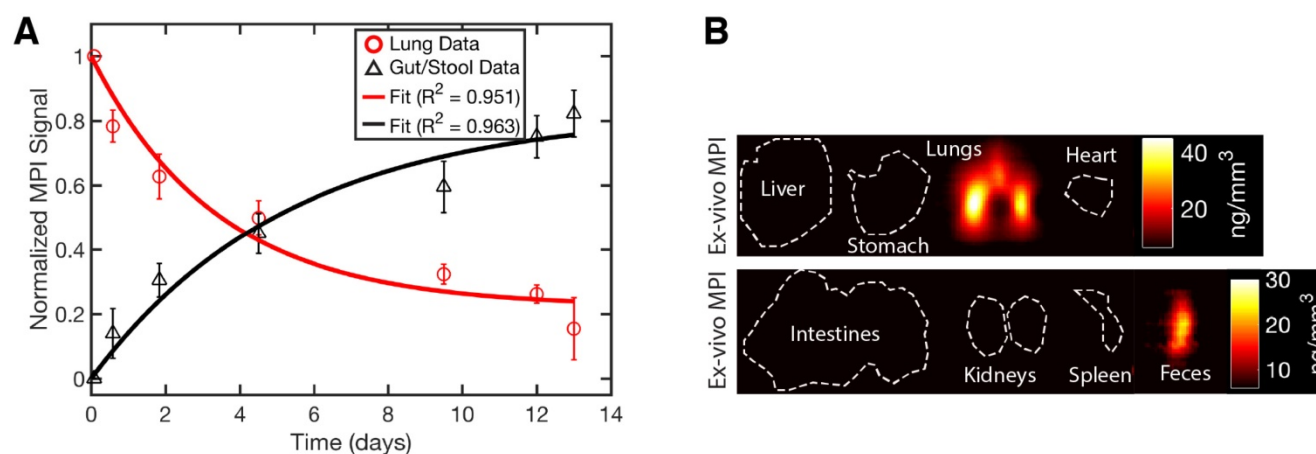
Figure 8. MPI quantification of the SPION biodistribution over time. (A) Changes in the biodistribution of SPIONs and two-compartment model fitting show that SPIONs are cleared from the lung and through the GI tract into excreta. The quantitative nature and high sensitivity of MPI shown here makes it a promising radiation-free alternative to radioaerosol procedures. **(B)** Ex vivo MPI validation shows SPIONs in only the lungs and excreta.

MPI quantification of mucociliary clearance

Because MPI is fully quantitative with zero depth attenuation [17], in addition to non-invasive tracking of the biodistribution through time, we were also able to model the SPION dynamics using a two-compartment model. The first compartment is the lung, while the gastrointestinal tract and the fecal excrement were combined into the second compartment. **Figure 8A** shows the biodistribution and compartmental fitting for Group C rats. First, the MPI signal was calibrated to a known concentration of SPION using a similar calibration curve to that in **Figure 3C**. Next, regions-of-interest (ROI) were identified for each compartment and the measured MPI concentration was subsequently averaged. The results were finally reported as net iron in each compartment (**Figure 8A**) and fitted to the exponential model described in prior work [20]. The equation used was:

$$Fe = Fe_{total} \cdot ((1 - k_1) \cdot e^{-k_2} + k_1)$$

$k_1 = 0.249$ and $k_2 = 0.261$ were obtained with the fitting ($R^2 = 0.955$). k_2 indicates the mucociliary time constant, while k_1 denotes the separation between the fast mucociliary clearance and slow (near constant) clearance term as explained in [20]. The results estimate the clearance half-life (without the offset term) as approximately 2.6 days.

The constant offset term can be attributed to deposition in regions (such as terminal bronchioles) with little cilia [61] that mainly use the slower alveolar macrophage pathway. The safety of iron oxide particles for lung deposition has also been demonstrated in prior studies [63].

Validation of SPION biodistribution

To confirm presence of SPIONs in the lung and feces, *ex vivo* MPI scans of all the organs were performed. The results at day 13 in **Figure 8B** show

that SPIONs were only in the lungs and the feces. Negligible signal (< 1% of lung signal) was observed in the stomach and intestines because the SPIONs were spread out over a large volume and slowly transferred over a long duration of digestion. Thus, the effective SPION concentration is very low, especially at the 13th day *ex vivo* time point when the transfer of SPIONs from the lung is much lower than the initial clearance rate. Prussian blue staining of lung sections show presence of SPIONs in the lung tissue, confirming delivery of SPION aerosol into the lung.

Discussion

This study is the first proof-of-concept of MPI for evaluating delivery efficiency of aerosols as well as tracking of inhaled therapeutics. We also further expanded on a prior clearance study [20] to visualize the *full* clearance pathway by detecting SPION clearance through the airways, gastrointestinal tract as well as in the fecal excrement, and finally performing two-compartment modeling of this clearance pathway and the associated kinetics. This monitoring of pulmonary delivery and clearance is important for slow-release formulations that need to resist mucociliary clearance and also for delivery confirmation in patients with diseased lungs who are likely to differ widely from predicted lung models.

The SPION properties can be tailored for MPI in the lung. The imaging performances of spatial resolution and sensitivity depend on the magnetic core. Attention should be given to phase purity [64] and the magnetic core size should be kept to ~25 nm for optimal imaging performance for single-core nanoparticles [53]. Multi-core nanoparticles should follow formulations similar to Resovist™ or recent multi-core SPION work [65]. In general, the nanoparticle coating thickness and material determine the colloidal stability, targeting and biodistribution properties, physiological half-life [66] and, in the case of the lung, ability to penetrate the blood-lung barrier [62].

While MPI is presented as a potential complement to radioaerosol techniques for clinical use, several limitations exist and continued development is required before MPI of SPIONs can be fully realized for clinical use in the lung. One limitation is that MPI is less sensitive (nanomolar sensitivity) than nuclear medicine (1−10 pM sensitivity for PET and 10−100 pM for SPECT) [5]. However, MPI is a new imaging technology and still has room for improvement since the hardware, scanning strategies and nanoparticles have not been exhaustively optimized yet. Recent hardware efforts to improve sensitivity are promising and a step towards picogram sensitivity [34]. The difference in sensitivity may be partially addressed by using larger doses of SPIONs (up to millimolar concentrations as approved by FDA [38]); whereas, due to radiation dose limits, nuclear medicine cannot perform the same increase in tracer dose. For instance, lung scintigraphy with 99mTc-MAA already gives ~185 MBq of radiation with a 11 pM radiotracer in a 1 mL injected volume [67].

Another limitation of MPI is that SPIONs are about 10–200 nm in hydrodynamic size and are larger than radioisotopes. Depending on the relative size of the SPION to the therapeutic agent, the valid timeframe for tracking of the therapeutic may be different. If controlled-release nanocarriers (comparable or larger in size than SPIONs) are being tracked rather than the small-molecule drug payload, then the SPIONs could be attached to the surface of these nanocarriers and the timeframe of tracking is valid throughout the entire in vivo timeframe of the nanocarrier. Such a study with MPI would be valuable to determine the residence time of the controlled-release nanocarrier in the lung and if it gets cleared out too quickly by mucociliary clearance.

In contrast, if a small-molecule therapeutic is of interest where the SPION is bigger than the therapeutic and tagging of the SPION to the therapeutic is difficult, then the valid timeframe is limited to only the initial aerosol deposition stage. The therapeutic will travel with the SPION in the aerosol droplet, and the initial deposition location is marked by the SPION. Over time, the SPION may be cleared by the mucociliary mechanism, while the small-molecule therapeutic diffuses into the bloodstream. As such, after the initial deposition point, MPI cannot track the drug in the bloodstream; therefore, the MPI scan should be performed immediately after pulmonary administration. Regardless, the ability for locating and quantifying the initial deposition of the aerosol (and thus quantifying the drug dosage available to alveoli for diffusion into the blood) is valuable for treatment planning. Further development of smaller, but still MPI-compatible nanoparticles that can tag onto small-sized therapeutics may enable MPI tracking of small therapeutics in the future. Such smaller nanoparticles may also be able to penetrate the blood-lung barrier and be targeted to specific organs, similar to how 5 nm gold nanoparticles can be non-invasively targeted to the brain [68]. Regardless, MPI can currently complement SPECT in the many current applications where large-size radioaerosols such as 99mTc albumin colloid aerosols are used [9].

While inhaling particulates has been known to cause damage to the lung such as pneumoconiosis,

pathogenicity is highly dependent on the characteristics of the particulates, especially the cytotoxicity or chemical features of the particulate itself as well as particle size-dependent activation of inflammation response [69]. With regard to the cytotoxicity of SPIONs, the SPIONs used in MPI are purely iron oxide (FDA approved for anemia therapy [38]) coated with a biocompatible coating, and as such, direct cytotoxicity is not expected. A prior study [70] showed that magnetite Fe_3O_4 nanoparticles (typically used in MPI) have negligible cytotoxicity for human alveolar type II-like epithelial cell line, A549, with merely 1–2% non-viable cells, a similar level to the negative control (~1%), while in contrast, CuO nanoparticles showed > 90% cytotoxicity. Other mechanisms of lung alveoli damage are related to the alveolar macrophages such as activation of oxidant (ROS) generation, stimulation of inflammatory cytokines and chemokines, and secretion of fibrogenic factors [69]. However, alveolar macrophage activation has a large dependence on particle size, where particle sizes less than 100 nm do not generate a large response [61]. MPI SPIONs are typically around or less than 100 nm, even with the biocompatible coating, and with further development, SPIONs can be made smaller to reduce alveolar macrophage response. Lastly, a key factor in pneumoconiosis development is the chronic exposure to silica or coal dust, which is on a different scale compared to single dose SPION administration in MPI scans.

Besides imaging, MPI has other characteristics that are potentially useful for various clinical applications. First, SPIONs can also provide relaxation information where relaxation refers to the delay in the magnetization response of the SPION. This delay and its associated time constant is affected by the physical environment of the SPIONs and can be leveraged as a sensor to enable *in vivo* sensing of tumor micro-environment factors such as viscosity and pH to provide additional contrast [41,71–73]. Second, the SPION magnetic core can also act as an actuator or heating agent to give a theranostic capability to the SPION imaging agent. This is especially useful since the same core can be used for imaging and therapy, and is thus very well-suited for image-guided therapy. Recent work has shown proof-of-concept of such image-guided therapy [50]. In addition, a method to exploit the MPI hardware to arbitrarily heat some SPIONs but not others in the body has been shown [50]. This enabled localized treatment of tumors (potentially lung tumors) while sparing other tissues with non-specific SPION uptake [47,50]. Furthermore, because SPIONs can be shifted by magnetomotive forces from magnetic gradient fields, the therapeutic aerosol can be additionally moved in an image-guided fashion to a target region of the lung, increasing therapeutic efficiency [43,74].

Conclusion

In this work, we have demonstrated proof-of-concept of MPI for various lung applications such as evaluation of efficiency and uniformity of aerosol delivery, tracking of the initial aerosolized therapeutic deposition *in vivo*, and sensitive visualization of the entire mucociliary clearance pathway from the lung, airways and through the gastrointestinal tract. While MPI is currently a preclinical imaging technique, the results show that MPI has the potential to be a future radiation-free complement to radioaerosol techniques in the clinic. With superb sensitivity and contrast as well as precise actuation of magnetic-based therapies, MPI is also a promising theranostics platform. We believe MPI can serve as a powerful method to improve the medical applications of SPIONs in lung imaging and therapy.

Abbreviations

CT: computed tomography; DOX HCl: Doxorubicin Hydrochloride; FFL: field-free line; FFR: field-free-region; FOV: field-of-view; ICG: Indocyanine Green; MPI: magnetic particle imaging; MRI: magnetic resonance imaging; PET: positron emission tomography; PSF: point-spread-function; SPECT: single-photon emission computed tomography; SPION: superparamagnetic iron-oxide nanoparticles.

Acknowledgements

Competing interests

E. Yu is an employee of Magnetic Insight Inc. and S. Conolly holds stock in the company. Magnetic Insight Inc. is a company that manufactures MPI scanners.

References

1. Ibrahim M, Verma R, Garcia-Contreras L. Inhalation drug delivery devices: technology update. Med Devices. 2015; 8: 131–139.
2. Kim D, Jeong YY, Jon S. A drug-loaded aptamer-gold nanoparticle bioconjugate for combined CT imaging and therapy of prostate cancer. ACS Nano. 2010; 4: 3689–3696.
3. Hyafil F, Cornily JC, Feig JE, Gordon R, Vucic E, Amirbekian V et al. Noninvasive detection of macrophages using a nanoparticulate contrast agent for computed tomography. Nat Med. 2007; 13: 636–641.

4. Kim J, Chhour P, Hsu J, Litt HI, Ferrari VA, Popovtzer R et al. Use of nanoparticle contrast agents for cell tracking with computed tomography. Bioconjug Chem. 2017; 28: 1581–1597.

5. James ML, Gambhir SS. A molecular imaging primer: modalities, imaging agents, and applications. Physiol Rev. 2012; 92: 897–965.

6. Newman SP. Lung distribution of inhaled drugs. Br J Clin Pharmacol. 2001; 52: 716–719.

7. Abdel-Dayem HM, Scott A, Macapinlac H, Larson S. Tracer imaging in lung cancer. Eur J Nucl Med. 1994; 21: 57–81.

8. Zheng B, Vazin T, Goodwill P, Conway A, Verma A, Saritas E et al. Magnetic particle imaging tracks the long-term fate of in vivo neural cell implants with high image contrast. Sci Rep. 2015; 5: 14055–14055.

9. Dolovich M, Labiris R. Imaging drug delivery and drug responses in the lung. Proc Am Thorac Soc. 2004; 1: 329–337.

10. Munkholm M, Nielsen KG, Mortensen J. Clinical value of measurement of pulmonary radioaerosol mucociliary clearance in the work up of primary ciliary dyskinesia. EJNMMI Res. 2015; 5: 118–118.

11. Marthin JK, Mortensen J, Pressler T, Nielsen KG. Pulmonary radioaerosol mucociliary clearance in diagnosis of primary ciliary dyskinesia. Chest. 2007; 132: 966–976.

12. Weers J, Metzheiser B, Taylor G, Warren S, Meers P, Perkins WR. A gamma scintigraphy study to investigate lung deposition and clearance of inhaled amikacinloaded liposomes in healthy male volunteers. J Aerosol Med Pulm Drug Deliv. 2009; 22: 131–138.

13. Labiris NR, Nahmias C, Freitag AP, Thompson ML, Dolovich MB. Uptake of 18-fluorodeoxyglucose in the cystic fibrosis lung: a measure of lung inflammation? Eur Respir J. 2003; 21: 848–854.

14. Nikolic B, Khosa F, Lin PJP, Khan AN, Sarwar S, Yam CS et al. Absorbed radiation dose in radiosensitive organs during coronary CT angiography using 320-MDCT: effect of maximum tube voltage and heart rate variations. AJR Am J Roentgenol. 2010; 195: 1347–1354.

15. Travis EL. Relative radiosensitivity of the human lung. In: Lett JT, Ed. Altman KI, Ed. Advances in Radiation Biology. 1st Ed. Internet. Elsevier; 1987: 205–238.

16. 43rd World Health Organization expert committee on specifications for pharmaceutical preparations. Radiopharmaceuticals. In: The International Pharmacopoeia. 4th Ed. World Health Organization; 2008: Supplementary Information 1–8.

17. Gleich B, Weizenecker J. Tomographic imaging using the nonlinear response of magnetic particles. Nature. 2005; 435: 1214–1217.

18. Zheng B, von See MP, Yu EY, Gunel B, Lu K, Vazin T et al. Quantitative magnetic particle imaging monitors the transplantation, biodistribution, and clearance of stem cells in vivo. Theranostics. 2016; 6: 291–301.

19. Zhou XY, Jeffris KE, Yu EY, Zheng B, Goodwill P, Nahid P et al. First in vivo magnetic particle imaging of lung perfusion in rats. Phys Med Biol. 2017; 62: 3510–3522.

20. Nishimoto K, Mimura A, Aoki M, Banura N, Murase K. Application of magnetic particle imaging to pulmonary imaging using nebulized magnetic nanoparticles. Open J Med Imaging. 2015; 5: 49–49.

21. Goodwill PW, Saritas EU, Croft LR, Kim TN, Krishnan KM, Schaffer DV et al. X-space MPI: magnetic nanoparticles for safe medical imaging. Adv Mater. 2012; 24: 3870–3877.

22. Saritas EU, Goodwill PW, Croft LR, Konkle JJ, Lu K, Zheng B et al. Magnetic particle imaging (MPI) for NMR and MRI researchers. J Magn Reson. 2013; 229: 116–126.

23. Knopp T, Biederer S, Sattel TF, Erbe M, Buzug TM. Prediction of the spatial resolution of magnetic particle imaging using the modulation transfer function of the imaging process. IEEE Trans Med Imaging. 2011; 30: 1284–1292.

24. Franke J, Heinen U, Lehr H, Weber A, Jaspard F, Ruhm W, Heidenreich M, Schulz V. System characterization of a highly integrated preclinical hybrid mpi-mri scanner. IEEE Trans Med Imaging. 2016; 35: 1993–2004.

25. Vogel P, Ruckert MA, Klauer P, Kullmann WH, Jakob PM, Behr VC. Superspeed traveling wave magnetic particle imaging. ieee trans magn. 2015; 51: 1–3.

26. Werner F, Gdaniec N, Knopp T. First experimental comparison between the Cartesian and the Lissajous trajectory for magnetic particle imaging. Phys Med Biol. 2017; 62: 3407–3421.

27. Rahmer J, Halkola A, Gleich B, Schmale I, Borgert J. First experimental evidence of the feasibility of multi-color magnetic particle imaging. Phys Med Biol. 2015; 60: 1775–1791.

28. Rahmer J, Weizenecker J, Gleich B, Borgert J. Signal encoding in magnetic particle imaging: properties of the system function. BMC Med Imaging. 2009; 9: 4–4.

29. Goodwill PW, Conolly SM. The X-space formulation of the magnetic particle imaging process: 1-D signal, resolution, bandwidth, SNR, SAR, and magnetostimulation. IEEE Trans Med Imaging. 2010; 29: 1851–1859.

30. Goodwill PW, Lu K, Zheng B, Conolly SM. An x-space magnetic particle imaging scanner. Rev Sci Instrum. 2012; 83: 033708–033708.

31. Goodwill PW, Konkle JJ, Zheng B, Saritas EU, Conolly SM. Projection x-space magnetic particle imaging. IEEE Trans Med Imaging. 2012; 31: 1076–1085.

32. Them K, Salamon J, Szwargulski P, Sequeira S, Kaul MG, Lange C, Ittrich H, Knopp T. Increasing the sensitivity for stem cell monitoring in system-function based magnetic particle imaging. Phys Med Biol. 2016; 61: 3279–3290.

33. Them K, Kaul MG, Jung C, Hofmann M, Mummert T, Werner F et al. Sensitivity enhancement in magnetic particle imaging by background subtraction. IEEE Trans Med Imaging. 2016; 35: 893–900.

34. Graeser M, Knopp T, Szwargulski P, Friedrich T, von Gladiss A, Kaul M. Towards picogram detection of superparamagnetic iron-oxide particles using a gradiometric receive coil. Sci Rep. 2017; 7: 6872–6872

35. Ludewig P, Gdaniec N, Sedlacik J, Forkert ND, Szwargulski P, Graeser M et al. Magnetic particle imaging for real-time perfusion imaging in acute stroke. ACS Nano. 2017; 11: 10480–10488.

36. Weissleder R, Stark DD, Engelstad BL, Bacon BR, Compton CC, White DL et al. Superparamagnetic iron oxide: pharmacokinetics and toxicity. AJR Am J Roentgenol. 1989; 152: 167–173.

37. Pouliquen D, Le Jeune JJ, Perdrisot R, Ermias A, Jallet P. Iron oxide nanoparticles for use as an MRI contrast agent: pharmacokinetics and metabolism. Magn Reson Imaging. 1991; 9: 275–283.

38. Lu M, Cohen MH, Rieves D, Pazdur R. FDA report: Ferumoxytol for intravenous iron therapy in adult patients with chronic kidney disease. Am J Hematol. 2010; 85: 315–319.

39. Song G, Chen M, Zhang Y, Cui L, Qu H, Zheng X et al. Janus iron oxides @ semiconducting polymer nanoparticle tracer for cell tracking by magnetic particle imaging. Nano Lett. 2018; 18: 182–189.

40. Salamon J, Hofmann M, Jung C, Kaul MG, Werner F, Them K et al. Magnetic particle / magnetic resonance imaging: in-vitro mpi-guided real time catheter tracking and 4d angioplasty using a road map and blood pool tracer approach. PLoS One. 2016; 11: e0156899.

41. Rahmer J, Wirtz D, Bontus C, Borgert J, Gleich B. Interactive magnetic catheter steering with 3-d real-time feedback using multi-color magnetic particle imaging. IEEE Trans Med Imaging. 2017; 36: 1449–1456.

42. Haegele J, Rahmer J, Gleich B, Borgert J, Wojtczyk H, Panagiotopoulos N et al. Magnetic particle imaging: visualization of instruments for cardiovascular intervention. Radiology. 2012; 265: 933–938.

43. Banura N, Murase K. Magnetic particle imaging for aerosol-based magnetic targeting. Jpn J Appl Phys. 2017; 56: 088001–088001.

44. Yu EY, Bishop M, Zheng B, Ferguson RM, Khandhar AP, Kemp SJ et al. Magnetic particle imaging: a novel in vivo imaging platform for cancer detection. Nano Lett. 2017; 17: 1648–1654.

45. Fidler F, Steinke M, Kraupner A, Gruttner C, Hiller KH, Briel A et al. Stem cell vitality assessment using magnetic particle spectroscopy. IEEE Trans Magn. 2015; 51: 1–4.

46. Orendorff R, Peck AJ, Zheng B, Shirazi SN, Ferguson RM, Khandhar AP et al. First in vivo traumatic brain injury imaging via magnetic particle imaging. Phys Med Biol. 2017; 62: 3501–3509.

47. Hensley D, Tay ZW, Dhavalikar R, Zheng B, Goodwill P, Rinaldi C et al. Combining magnetic particle imaging and magnetic fluid hyperthermia in a theranostic platform. Phys Med Biol. 2017; 62: 3483–3500.

48. Murase K, Takata H, Takeuchi Y, Saito S. Control of the temperature rise in magnetic hyperthermia with use of an external static magnetic field. Phys Med. 2013; 29: 624–630.

49. Murase K, Aoki M, Banura N, Nishimoto K, Mimura A, Kuboyabu T et al. Usefulness of magnetic particle imaging for predicting the therapeutic effect of magnetic hyperthermia. Open Journal of Medical Imaging. 2015; 05: 85–99.

50. Tay ZW, Chandrasekharan P, Chiu-Lam A, Hensley DW, Dhavalikar R, Zhou XY et al. Magnetic particle imaging-guided heating in vivo using gradient fields for arbitrary localization of magnetic hyperthermia therapy. ACS Nano. 2018; 12: 3699–3713.

51. Yu EY, Chandrasekharan P, Berzon R, Tay ZW, Zhou XY, Khandhar AP et al. Magnetic particle imaging for highly sensitive, quantitative, and safe in vivo gut bleed detection in a murine model. ACS Nano. 2017; 11: 12067–12076.

52. Tay ZW, Goodwill PW, Hensley DW, Taylor LA, Zheng B, Conolly SM. A High-throughput, arbitrary-waveform, mpi spectrometer and relaxometer for comprehensive magnetic particle optimization and characterization. Sci Rep. 2016; 6: 34180–34180.

53. Tay ZW, Hensley DW, Vreeland EC, Zheng B, Conolly SM. The relaxation wall: experimental limits to improving mpi spatial resolution by increasing nanoparticle core size. Biomed Phys Eng Express. 2017; 3: 035003–035003.

54. Sagnella SM, Duong H, MacMillan A, Boyer C, Whan R, McCarroll JA, Davis TP, Kavallaris M. Dextran-based doxorubicin nanocarriers with improved tumor penetration. Biomacromolecules. 2014; 15: 262–275.

55. Wang Y-XJ. Superparamagnetic iron oxide based MRI contrast agents: Current status of clinical application. Quant Imaging Med Surg. 2011; 1: 35–40.

56. Longest PW, Azimi M, Hindle M. Optimal delivery of aerosols to infants during mechanical ventilation. J Aerosol Med Pulm Drug Deliv. 2014; 27: 371–385.

57. Kleinstreuer C, Zhang Z. Optimal drug-aerosol delivery to predetermined lung sites. J Heat Transfer. 2011; 133: 011002–011002.

58. Newman SP. Aerosol deposition considerations in inhalation therapy. Chest. 1985; 88: 152S–160S.

59. Cheng YS. Mechanisms of pharmaceutical aerosol deposition in the respiratory tract. AAPS Pharm Sci Tech. 2014; 15: 630–640.

60. Semmler M, Seitz J, Erbe F, Mayer P, Heyder J, Oberdörster G et al. Long-term clearance kinetics of inhaled ultrafine insoluble iridium particles from the rat lung, including transient translocation into secondary organs. Inhal Toxicol. 2004; 16: 453–459.

61. Tandel H, Florence K, Misra A. Protein and peptide delivery through respiratory pathway. In: Misra A, Ed. Challenges in Delivery of Therapeutic Genomics and Proteomics. 1st ed. Elsevier; 2010: 429–479.

62. Miller MR, Raftis JB, Langrish JP, McLean SG, Samutrtai P, Connell SP et al. Inhaled nanoparticles accumulate at sites of vascular disease. ACS Nano. 2017; 11: 4542–4552.

63. Möller W, Häussinger K, Winkler-Heil R, Stahlhofen W, Meyer T, Hofmann W et al. Mucociliary and long-term particle clearance in the airways of healthy nonsmoker subjects. J Appl Physiol. 2004; 97: 2200–2206.

64. Hufschmid R, Arami H, Ferguson RM, Gonzales M, Teeman E, Brush LN et al. Synthesis of phase-pure and monodisperse iron oxide nanoparticles by thermal decomposition. Nanoscale. 2015; 7: 11142–11154.

65. Kratz H, Taupitz M, Ariza de Schellenberger A, Kosch O, Eberbeck D, Wagner S et al. Novel magnetic multicore nanoparticles designed for MPI and other biomedical applications: From synthesis to first in vivo studies. PLoS One. 2018; 13: e0190214.

66. Keselman P, Yu EY, Zhou XY, Goodwill PW, Chandrasekharan P, Ferguson RM et al. Tracking short-term biodistribution and long-term clearance of SPIO tracers in magnetic particle imaging. Phys Med Biol. 2017; 62: 3440–3453.

67. Picano E, Vañó E, Rehani MM, Cuocolo A, Mont L, Bodi V et al. The appropriate and justified use of medical radiation in cardiovascular imaging: a position document of the ESC associations of cardiovascular imaging, percutaneous cardiovascular interventions and electrophysiology. Eur Heart J. 2014; 35: 665–672.

68. Raliya R, Saha D, Chadha TS, Raman B, Biswas P. Non-invasive aerosol delivery and transport of gold nanoparticles to the brain. Sci Rep. 2017; 7: 44718.

69. Castranova V, Vallyathan V. Silicosis and coal workers' pneumoconiosis. Environ Health Perspect. 2000; 108: 675–684.

70. Karlsson HL, Gustafsson J, Cronholm P, Möller L. Size-dependent toxicity of metal oxide particles – a comparison between nano- and micrometer size. Toxicol Lett. 2009; 188:112–118.

71. Utkur M, Muslu Y, Saritas EU. Relaxation-based viscosity mapping for magnetic particle imaging. Phys Med Biol. 2017; 62: 3422–3439.

72. Muslu Y, Utkur M, Demirel OB, Saritas EU. Calibration-free relaxation-based multi-color magnetic particle imaging. IEEE Trans Med Imag 2018; [Epub ahead of print].

73. Gandhi S, Arami H, Krishnan KM. Detection of cancer-specific proteases using magnetic relaxation of peptide-conjugated nanoparticles in biological environment. Nano Lett. 2016; 16: 3668–3674.

74. Kuboyabu T, Ohki A, Banura N, Murase K. Usefulness of magnetic particle imaging for monitoring the effect of magnetic targeting. Open Journal of Medical Imaging. 2016; 6: 33–33.